Nonlinear harmonic spectra in the bilayer van der Waals antiferromagnets CrX_3

Y. Q. Liu [1], M. S. Si [1,*] and G. P. Zhang [2,†]

[1] *School of Materials and Energy, Lanzhou University, Lanzhou 730000, China*

[2] *Department of Physics, Indiana State University, Terre Haute, Indiana 47809, USA*

(Received 28 September 2023; revised 7 February 2024; accepted 14 February 2024; published 4 March 2024)

Bilayer antiferromagnets CrX_3 (X = Cl, Br, and I) are promising materials for spintronics and optoelectronics that are rooted in their peculiar electronic structures. However, their bands are often hybridized from the interlayer antiferromagnetic ordering, thus they are difficult to disentangle by traditional methods. In this work, we show theoretically that nonlinear harmonic spectra can reveal subtle differences in their electronic states. In contrast to prior nonlinear optical studies, which often use one- or two-photon energies, we systematically study the wavelength-dependent nonlinear harmonic spectra realized by hundreds of individual dynamical simulations under changed photon energies. Through turning on and off some excitation channels, we can pinpoint every dipole-allowed transition that largely contributes to the second and third harmonics. With the help of momentum matrix elements, highly entangled resonance peaks at a higher energy above the band edge can be assigned to specific transitions between the valence bands and three separate regions of conduction bands. Our findings demonstrate a feasible means to detect very complex electronic structures in an important family of two-dimensional antiferromagnets.

DOI: 10.1103/PhysRevB.109.094301

I. INTRODUCTION

Among the two-dimensional van der Waals (vdW) magnetic materials discovered so far, bilayers CrX_3 (X = Cl, Br, and I) stand out as a key group of materials for spintronics and optoelectronics. They exhibit remarkable electronic and optical properties [1–5] that are unparalleled by other materials. The interlayer magnetic coupling between adjacent ferromagnetic monolayers of CrX_3 can be manipulated by applying external fields [6–10] or adjusting the stacking patterns [11,12]. Different interlayer magnetic couplings in bilayers CrX_3 are vital to tunnel magnetoresistance. More notably, bilayers CrX_3 provide an excellent platform for studying light-matter interactions such as the magneto-optic Kerr effect [13], magnetic circular dichroism [14], polarized photoluminescence [15], and second-harmonic generation (SHG) [16,17]. Further progress is not possible without a detailed understanding of their electronic states. Nonlinear optical techniques such as SHG, third or high harmonic generation (HHG) [18–23], and delivering attosecond laser pulses [24] are methods of choice. Based on the three-step model proposed by Vampa *et al.* [25], the valence and conduction bands during excitation are selected by the wavelength of a laser pulse. They have shown that the interband contribution is more pronounced with a shorter wavelength [25]. In ZnO, high harmonic spectra up to 25th order are generated by a driving laser with wavelength of 3250 nm, where the maximum cutoff is determined by the maximum energy difference between the valence and conduction bands [26]. Decreasing the wavelength to 800 nm, Osika *et al.* predict that the cutoff moves to the lower harmonics [27]. This wavelength dependence is confirmed in a model system [28]. In monolayer MoS_2, Liu *et al.* report that the even and odd harmonics are extended to the 13th order under a wavelength of 4133 nm. It is found that the even-order harmonic intensity is much smaller than that of the odd-order harmonic intensity, implying different excited origins of these two kinds of harmonics [19]. This conclusion is also theoretically confirmed from the decreased wavelength [29]. All the above studies reveal that the underlying physics of nonlinear optical response depends on the wavelength of the applied laser pulses. In fact, both experimental and theoretical studies have already pointed out that the wavelength dependence of harmonics is a key characteristic of solids, which is different from the cases in atoms and small molecules. In experiments, Sun *et al.* extracted SHG susceptibilities $|\chi^{(2)}_{xxx}|$ and $|\chi^{(2)}_{xyy}|$ of bilayer CrI_3 by scanning 17 excitation wavelengths in the range from 800 to 1040 nm [16]. At relatively low photon energies, the intensities of the resonance peaks are weak, but as the photon energy gradually increases, their intensities become stronger. However, due to a small number of photon energies used, some important resonance peaks may be missed, which is crucial for analyzing the electronic state of the material. This motivates us to carry out a systematic study.

In this work, we demonstrate that nonlinear harmonics in a group of bilayers CrX_3 can pinpoint electronic states, state by state, by scanning the photon energy between 0.3 and 1.4 eV in steps of 0.01 or 0.02 eV, rather than one- or two-photon energies often employed. The first peaks of the second-harmonic spectra, resulting from the real electronic transitions between the valence and conduction bands, are the onset of the optical band gaps for each CrX_3. As the band gap gradually decreases with halogens down the Periodic Table, the peaks redshift. Above the first peak, complex peaks are attributed to the resonance transitions. We verify the reliability of the second-harmonic spectra by continuous wave (cw) SHG. For $CrCl_3$, the second-harmonic peaks, consisting of three eigenpeaks I,

*sims@lzu.edu.cn

†guo-ping.zhang@outlook.com

II, and III, are associated with the conduction bands between 1.6 and 2.0 eV, called region 1 or R_1. These three eigenpeaks are dominated by the transitions between the valence bands and the conduction bands in R_1. The eigenpeaks result from the dipole-allowed transitions, where the incident photon energy matches the energy difference between the valence and conduction bands, and the corresponding momentum matrix elements are also large. The same is true for the other two materials $CrBr_3$ and CrI_3. In the third-harmonic spectra, 15 transition channels are identified from the same strategy. Our study demonstrates the potential power of nonlinear harmonic spectra by mapping out the electronic states through a systematic scan of many incident photon energies, which complements the experimental studies [16].

The rest of the paper is arranged as follows. In Sec. II, we present our theoretical methods. Then, the results and discussions are given in Sec. III. Section IV focuses on the third harmonic and the underlying physical picture. Finally, we conclude our work in Sec. V.

II. THEORETICAL METHODS

We employ the first-principles method combined with the Liouville equation to simulate the dynamical nonlinear optical response. The electronic structures for bilayers CrX_3 are calculated in the framework of density functional theory (DFT), which is implemented in WIEN2K [30–32]. We employ the generalized gradient approximation (GGA) for exchange-correlation potential in the form of Perdew-Burke-Ernzerhof (PBE) [33]. We self-consistently solve the Kohn-Sham equation [34–36] as

$$\left[-\frac{\hbar^2}{2m_e}\nabla^2 + V_{\text{eff}}(\mathbf{r})\right]\psi_{n\mathbf{k}}(\mathbf{r}) = E_{n\mathbf{k}}\psi_{n\mathbf{k}}(\mathbf{r}), \tag{1}$$

where $\psi_{n\mathbf{k}}(\mathbf{r})$ is the Bloch wave function of band index n at crystal momentum $\mathbf{k}$, and $E_{n\mathbf{k}}$ denotes the corresponding eigenvalue. The first and second terms of the Hamiltonian are the kinetic energy and the Kohn-Sham effective potential, respectively. In our calculations, the plane-wave expansion is determined by a cutoff parameter $R_{mt}K_{\max} = 7.0$. Dense k-sample points with $32\times32\times1$ are used to ensure the convergence of the total energy. All calculations are performed under the spin-orbit coupling (SOC), which are realized through the second variational method. The experimental lattice constants of 5.94, 6.30, and 6.87 Å are used for $CrCl_3$, $CrBr_3$, and CrI_3, respectively [2,37,38]. The AB-stacking order is taken for bilayers CrX_3. The unit cell contains four Cr atoms and twelve X atoms. The interlayer distances for $CrCl_3$, $CrBr_3$, and CrI_3 are 5.76, 6.05, and 6.82 Å, respectively [12]. To mimic the two-dimensional geometry, a vacuum layer of height 16 Å is inserted between the bilayers along the z direction.

To obtain HHG, we first construct the density matrix of the ground state as $\rho_0 = |\psi_{n\mathbf{k}}(\mathbf{r})\rangle\langle\psi_{n\mathbf{k}}(\mathbf{r})|$. Then, the dynamic density matrix can be obtained by numerically solving the time-dependent Liouville equation [39–41]

$$i\hbar\langle m\mathbf{k}|\partial\rho/\partial t|n\mathbf{k}\rangle = \langle m\mathbf{k}|[\mathcal{H},\rho]|n\mathbf{k}\rangle, \tag{2}$$

where ρ is the time-dependent density matrix, and a generic Hamiltonian is expressed as $\mathcal{H} = \mathcal{H}_0 + \mathcal{H}_I$. $\mathcal{H}_0$ is the system Hamiltonian. $\mathcal{H}_I$ is the interaction Hamiltonian between the laser field and the system: $\mathcal{H}_I = \frac{e}{m_e}\hat{\mathbf{P}}\cdot\mathbf{A}(t)$, where $\hat{\mathbf{P}}$ is the momentum operator, and $\mathbf{A}(t)$ represents the vector potential of the laser field. The detailed vector potential used in this work is $\mathbf{A}(t) = A_0 e^{-t^2/\tau^2}[\cos(\omega t)\hat{\mathbf{n}}]$, with $\hat{\mathbf{n}}$ being the unit vector of laser pulse polarization. The vector potential amplitude is taken as $A_0 = 0.03$ Vfs/Å and the duration τ is set to 60 fs. The incident photon energies $\hbar\omega$ range from 0.3 to 1.4 eV at steps of 0.01 or 0.02 eV. After obtaining the time-dependent density matrix ρ, we can calculate the expectation value of momentum operator [42] through $\mathbf{P}(t) = \Sigma_{\mathbf{k}}\text{Tr}[\rho_{\mathbf{k}}(t)\hat{\mathbf{P}}_{\mathbf{k}}]$ with $\hat{\mathbf{P}}_{\mathbf{k}} = -i\hbar\nabla$. Finally, we get the harmonic spectra by Fourier transforming $\mathbf{P}(t)$ into the frequency domain by $\mathbf{P}(\omega) = \int_{-\infty}^{\infty}\mathbf{P}(t)e^{i\omega t}\mathcal{W}(t)dt$, with ω being the harmonic frequency and $\mathcal{W}(t)$ the window function.

III. RESULTS AND DISCUSSIONS

A. Static properties and cw SHG

The crystal structure of bilayers CrX_3 is displayed in the bottom panel of Fig. 1(a). Bilayers CrX_3 have an S_6 point group. There are six symmetry operations that can be generated by the inversion symmetry $\mathcal{I}$ and the threefold rotational symmetry C_3 with the trigonal axis as the z axis. It should be noted that $\mathcal{I}$ is broken from the interlayer antiferromagnetic (AFM) ordering with the magnetization of the monolayer along the z axis, denoted as AFM-z. Under AFM-z, the combined symmetry $\mathcal{IT}$ is preserved with $\mathcal{T}$ being the time-reversal symmetry. The band structure of $CrCl_3$ is given in Fig. 1(b). All those bands are doubly degenerate, which is protected by $\mathcal{IT}$ [43]. The valence bands near the Fermi level are mainly from the Cr-d orbitals. Below them, the bands mainly come from the Cl-p orbitals. Above the Fermi level, the conduction bands mainly come from the Cr-d orbitals, which are grouped into three separate regions $R_1 - R_3$.

The nonlinear optical response has the potential to reveal the physical properties of a material from the light-matter interaction. The resonant enhancement is crucial to detect the band structure of a material, and it has the most important contribution to the susceptibilities [44–46]. Based on the three-level model as schematically shown in the inset of Fig. 1(c), the second-order susceptibility of cw SHG can be obtained as

$$\chi^{(2)}_{ijk} = \frac{Ne^3}{2\epsilon_0\hbar^2}\sum_{lmn}\rho^{(0)}_{ll}\left[\frac{r^i_{ln}r^j_{nm}r^k_{ml}}{(\omega_{nl}-2\omega-i\eta)(\omega_{ml}-\omega-i\eta)} + \frac{r^k_{ln}r^i_{nm}r^j_{ml}}{(\omega_{mn}-2\omega-i\eta)(\omega_{nl}+\omega+i\eta)}\right.$$
$$\left. + \frac{r^j_{ln}r^i_{nm}r^k_{ml}}{(\omega_{nm}+2\omega+i\eta)(\omega_{ml}-\omega-i\eta)} + \frac{r^k_{ln}r^j_{nm}r^i_{ml}}{(\omega_{ml}+2\omega+i\eta)(\omega_{nl}+\omega+i\eta)}\right] + (j\leftrightarrow k), \tag{3}$$

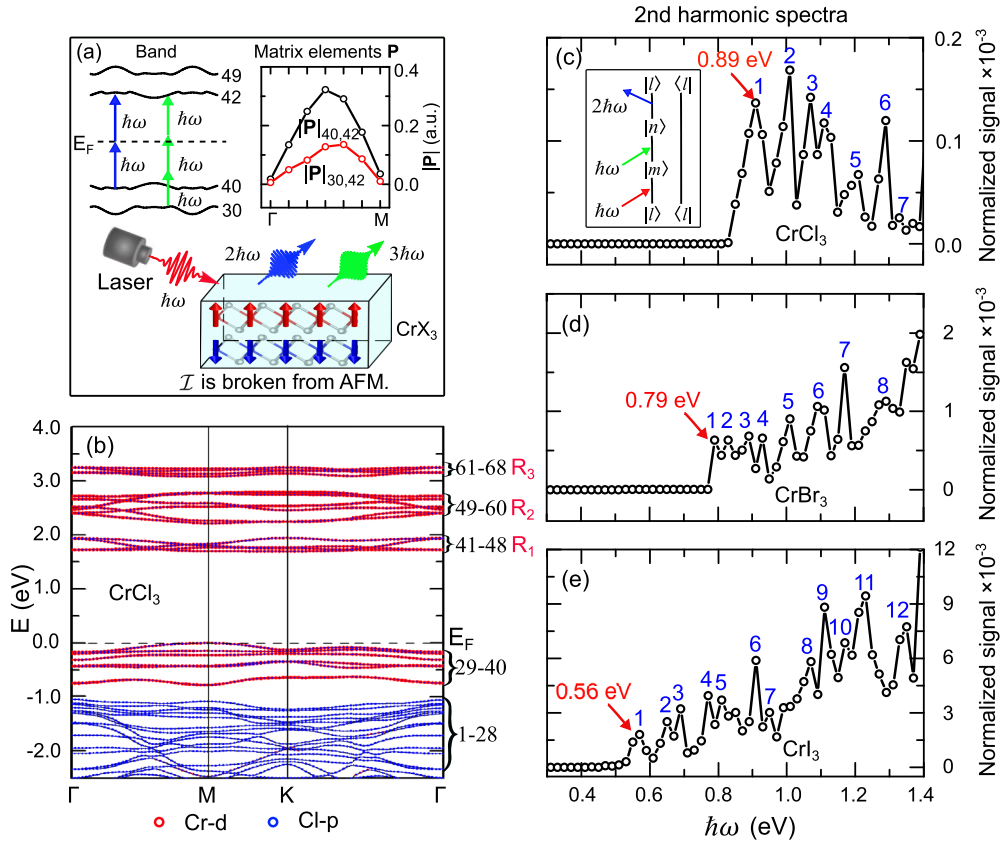

FIG. 1. (a) A schematic diagram of nonlinear optical responses in bilayer CrX_3, which are related to the band structure and the momentum matrix elements $\mathbf{P}$. $|\mathbf{P}|_{40,42}$ between the bands 40 and 42 is larger than $|\mathbf{P}|_{30,42}$ along Γ-M in bilayer $CrCl_3$. (b) Orbital-resolved band structure for bilayer $CrCl_3$, where the red and blue circles represent the Cr-d and Cl-p orbitals, respectively. The band indices 1–68 are marked on the right side of this figure. The conduction bands are divided into three individual regions $R_1 - R_3$. (c) The second-harmonic spectra as a function of photon energy for bilayer $CrCl_3$. The blue numbers near the peaks represent the peak indices and the red number is the photon energy of the first peak. The inset shows the conventional double-sided Feynman diagram corresponding to the first term in Eq. (1). The Feynman diagram has two lines of propagation, one for the $|l\rangle$ side of $\rho^{(0)}_{ll}$ and the other for the $\langle l|$ side. The red, green, and blue arrows correspond to the input photon energies $\hbar\omega$ and $\hbar\omega$ and the output photon energies $2\hbar\omega$, respectively. The energy conservation relation $\hbar\omega + \hbar\omega = 2\hbar\omega$ is satisfied. (d) and (e) The second-harmonic spectra as a function of photon energy for bilayers $CrBr_3$ and CrI_3, respectively.

where subscripts i, j, and k of $\chi^{(2)}_{ijk}$ denote the Cartesian indices, N is the atomic density, $\rho^{(0)}_{ll}$ is the initial population for the state $|l\rangle$, $\omega_{nl} = \omega_n - \omega_l$, with $\hbar\omega_n$ being the energy of band n, $\hbar\omega$ is the photon energy, r_{ln} is the matrix element of the position operator between electronic states $|l\rangle$ and $|n\rangle$, and η is the damping parameter [47,48]. The notation $(j \leftrightarrow k)$ means an exchange of the two Cartesian directions. The first term in Eq. (1) can be visualized by the double-sided Feynman diagram, as shown in the inset of Fig. 1(c). The resonant enhancement can be understood from its denominator, where two terms $(\omega_{nl} - 2\omega - i\eta)$ and $(\omega_{ml} - \omega - i\eta)$ are involved. When $2\hbar\omega = \hbar\omega_{nl}$ or $\hbar\omega = \hbar\omega_{ml}$, the cw SHG susceptibility has two typical peaks: one at $\hbar\omega_{ml}$ for the transition $|m\rangle \to |l\rangle$ and the other at half of $\hbar\omega_{nl}$ for the transition $|n\rangle \to |l\rangle$. Our peaks in cw SHG originate from these resonant contributions. However, for the degenerate bands, $\hbar\omega_{nl}$ and $2\hbar\omega_{ml}$ are usually small. This will lead to a divergence when the photon energy $\hbar\omega$ approaches zero [49]. We are aware that the low-frequency divergence in the nonlinear optical response depends on the gauges used. Although the velocity gauge can handle the low-frequency divergence, it is problematic to truncate the summation of multiple bands [50,51]. On the other hand, the length gauge takes the k derivative instead of the position operator to account for the local effect of wave functions, but to numerically compute it is challenging [52]. Thus, our dynamical nonlinear response approach is a better way to overcome limitations, as discussed below.

B. Dynamical response

In the perturbation theory, the first-order density matrix $\rho^{(1)}$ is computed as

$$i\hbar\dot{\rho}^{(1)} = [H_0, \rho^{(1)}] + [H_I, \rho^{(0)}], \tag{4}$$

where H_0 is the unperturbed Hamiltonian and H_I is the interaction between the laser field and the system. The second-order density matrix is given by

$$i\hbar\dot{\rho}^{(2)} = [H_0, \rho^{(2)}] + [H_I, \rho^{(1)}]. \tag{5}$$

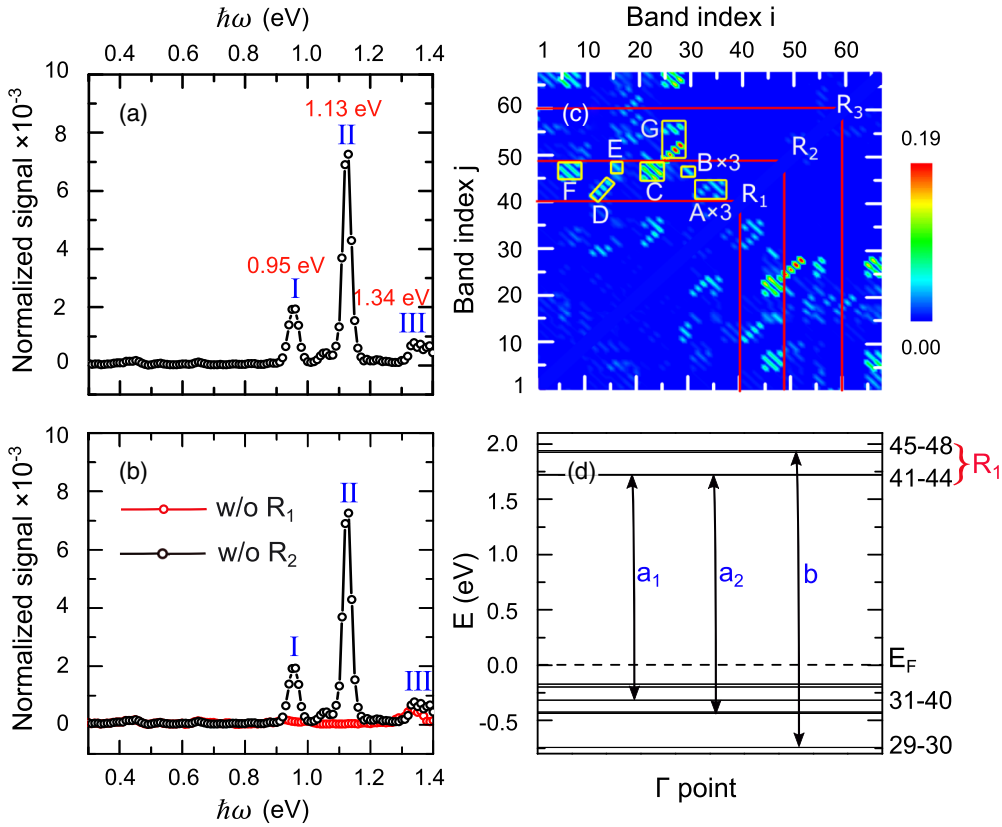

FIG. 2. (a) The second-harmonic spectra as a function of photon energy at Γ for bilayer $CrCl_3$. The blue and red numbers near each peak represent the peak indices and the corresponding photon energies, respectively. (b) The second-harmonic spectra as a function of photon energy excluding R_1 (red line) and R_2 (black line) in the conduction bands. (c) The absolute value of the momentum matrix elements $|\mathbf{P}|$ for bands 1–68 in bilayer $CrCl_3$. (d) The energy diagram at Γ for bilayer $CrCl_3$, where the arrows denote transitions with large $\mathbf{P}$, and the letters on the arrow label the different transitions.

In the interaction picture, $\rho^{(2)}$ is

$$\rho^{(2)}(t) = \frac{1}{(i\hbar)^2}\int_{-\infty}^{t} dt_1 \int_{-\infty}^{t_1} dt_2 [H_I(t_1), [H_I(t_2), \rho_0]]. \quad (6)$$

Because the system response is in the expectation value of the momentum operator through the trace $\mathrm{Tr}(\rho\hat{\mathbf{P}})$, the second-order response depends on $\mathbf{P}_{ij}$. Although we numerically solve the Liouville equation exactly, this dependence is useful for our purpose, as illustrated in Fig. 1(a), where the nonlinear response is linked to the product of multiple momentum transition matrix elements. In addition, the nonlinear optical response based on the time-dependent density matrix has no limitation of the energy difference between electronic states. This leads to a relatively accurate result near the zero-photon frequency. If the excitonic effect is considered, additional resonant peaks would appear in the low-frequency range [53,54], which is beyond the scope of our current work. A normal practice in HHG is to choose one- or two-photon energies and then to Fourier transform the expectation value of momentum operator $\mathbf{P}(t) = \Sigma_{\mathbf{k}}\mathrm{Tr}[\rho_{\mathbf{k}}(t)\hat{\mathbf{P}}_{\mathbf{k}}]$ with $\hat{\mathbf{P}}_{\mathbf{k}} = -i\hbar\nabla$ to get the spectrum as $\mathbf{P}(\omega) = \int_{-\infty}^{\infty}\mathbf{P}(t)e^{i\omega t}dt$. But this has a deficiency. Because of the energy-time uncertainty relation in the Fourier transform, one cannot resolve harmonic peaks energetically down to 0.2 eV, except that one uses an extremely long pulse. Higher harmonics need many more parameters, and even within the perturbation theory their formulas become overly convoluted. This requires a different strategy.

C. Physics of even harmonics

Nonmagnetic bilayers CrX_3 remain centrosymmetric as their monolayers. If we consider the magnetic structures of Cr atoms, the inversion symmetry is broken from the interlayer antiferromagnetic order as the top layer with spin-up magnetic orders is changed to the bottom layer with the same spin-up magnetic orders under the spatial inversion operator ($\vec{r} \to -\vec{r}$) and vice versa, as shown in the bottom panel of Fig. 1(a). Meanwhile, the time-reversal symmetry is also broken from this antiferromagnetic order. According to the electric-dipole approximation, the even harmonics are allowed and also time-nonreciprocal, usually denoted as c-type [16]. Our calculated HH spectra did include both the odd and even harmonics and confirm this symmetry analysis, as shown in Fig. S1(c) of the Supplemental Material (SM) [55]. When the interlayer magnetic order is changed to be ferromagnetic, the spatial inversion symmetry is recovered as the top layer with spin-up magnetic orders is identical to the bottom layer under $\vec{r} \to -\vec{r}$. As a result, the even harmonics disappear, as shown in Fig. S1(d) [55]. Thus, these unique magnetic structures in

bilayers CrX_3 can be used to study the magnetization-mediated nonlinear harmonic spectra.

D. Photon energy scan

We scan the incident photon energies $\hbar\omega$ between 0.3 and 1.4 eV in steps of 0.02 eV to obtain nonlinear harmonic spectra. Figure 1(c) shows the second-harmonic spectra of bilayer $CrCl_3$. When $\hbar\omega$ is below 0.9 eV, the second-harmonic signals are negligible. We understand the reason behind this. $2\hbar\omega$ corresponds to the energy 1.8 eV, about 0.1 eV above the band gap of $CrCl_3$, so only virtual transitions occur, which explains the negligible harmonic signal. When the photon energy is above 0.9 eV, the real electron transitions touch the bands. Thus, the first peak in this second-harmonic spectrum can be regarded as an indicator of the band gap of a material. This is also the case for $CrBr_3$ and CrI_3, as displayed in Figs. 1(d) and 1(e).

As the photon energy increases, an additional six peaks 2−7 appear for $CrCl_3$, as shown in Fig. 1(c). Four of them, peaks 2−4 and 6, are comparable to the first peak. Peaks 5 and 7 have smaller amplitudes and peaks at 1.21 and 1.33 eV, respectively. It should be noted that most of these characteristic peaks also appear in cw SHG, as discussed in the SM [55] (see also Refs. [56–60] therein). For $CrBr_3$, the first peak appears at $\hbar\omega = 0.79$eV, as shown in Fig. 1(d), thus $2\hbar\omega = 1.58$eV is only 0.16 eV above the band gap of 1.42 eV for $CrBr_3$. Seven peaks, $2-8$, appear after peak 1. For CrI_3, more peaks appear, but they have much stronger amplitudes, as shown in Fig. 1(e).

E. Understanding the complex spectra

The peaks in Figs. 1(c)–1(e) are very complex, but they offer an opportunity to demonstrate the power of harmonic generation. In the following, we use an even finer step of 0.01 eV to scan the photon energy from 0.3 to 1.4 eV. This requires 110 separate runs. We focus on the second-harmonic spectra at Γ. Figure 2(a) shows that the harmonic amplitude is small until the photon energy reaches 0.95 eV, where peaks I−III, called eigenpeaks, appear. Peak I has a small blueshift compared with the result in Fig. 1(c), because the conduction-band minimum and the valence-band maximum of $CrCl_3$ are not at Γ. Peak II appears at 1.13 eV, and its amplitude is large, indicating an enhanced transition at this energy difference of 2.26 eV. Peak III at 1.34 eV is very small. The difference among these eigenpeak amplitudes implies the different transitions between the valence and conduction bands. As seen above, we divide the conduction bands of $CrCl_3$ into three regions $R_1 - R_3$, so we can determine their separate effects on the harmonic amplitude. We first exclude R_1 and find that peaks I and II disappear, and peak III decreases [the red line of Fig. 2(b)]. This means that peaks $\mathrm{I} - \mathrm{III}$ are significantly affected by the transitions between the valence bands and conduction bands in R_1. Excluding only R_2 hardly changes anything [the black line of Fig. 2(b)]. When only R_3 is excluded, these three peaks are also intact. Therefore, eigenpeaks $\mathrm{I} - \mathrm{III}$ in the second-harmonic spectra are mainly contributed by the transitions between the valence bands and conduction bands in R_1.

TABLE I. Transitions in regions A–G in Fig. 2(c), with large momentum matrix elements $|\mathbf{P}|$. The corresponding transition energies match the harmonic energies of the eigenpeaks, where I–III denote the peaks in the second-harmonic spectra and 1–7 denote those eigenpeaks in the third-harmonic spectra. ΔE and $\hbar\omega$ represent the transition and photon energies, respectively, in units of eV. The momentum matrix elements are in units of atomic unit (a.u.).

Region	Transition	$\lvert\mathbf{P}\rvert$	ΔE	Peak	$\hbar\omega$ ($2\hbar\omega/3\hbar\omega$)
A	$35, 36 \to 41, 42$	0.03	2.02 (a_1)	I	0.95 (1.90)
	$31, 32 \to 43, 44$	0.03	2.16 (a_2)	II	1.13 (2.26)
B	$29, 30 \to 47, 48$	0.03	2.66 (b)	III	1.34 (2.68)
C	$23, 24 \to 45, 46$	0.18	3.07 (c_1)	1	1.02 (3.06)
	$23, 24 \to 47, 48$	0.15	3.08 (c_2)	1	
	$21, 22 \to 45, 46$	0.13	3.14 (c_3)	2	1.05 (3.15)
	$21, 22 \to 47, 48$	0.15	3.15 (c_4)	2	
D	$11, 12 \to 41, 42$	0.11	3.20 (d_1)	2	1.05 (3.15)
	$13, 14 \to 43, 44$	0.11	3.21 (d_2)	2	
E	$15, 16 \to 48, 47$	0.09	3.26 (e)	3	1.12 (3.36)
F	$7, 8 \to 45, 46$	0.11	3.88 (f_1)	6	1.30 (3.90)
	$7, 8 \to 47, 48$	0.11	3.89 (f_2)	6	
	$5, 6 \to 45, 46$	0.12	3.98 (f_3)	7	1.33 (3.99)
	$5, 6 \to 47, 48$	0.11	3.99 (f_4)	7	
G	$27, 28 \to 51, 52$	0.23	3.46 (g_1)	4	1.15 (3.45)
	$25, 26 \to 49, 50$	0.20	3.53 (g_2)	4	
	$27, 28 \to 55, 56$	0.13	3.56 (g_3)	4	
	$25, 26 \to 55, 56$	0.11	3.65 (g_4)	5	1.23 (3.69)

All the above discussions tell us that these eigenpeaks require resonant transitions, where the incident photon energy must match the transition energy. However, this is not the entire story. Another criterion for these eigenpeaks is large momentum matrix elements between transition bands. We calculate the momentum matrix elements for those bands that are indexed in 1–68 for bilayer $CrCl_3$, as shown in Fig. 2(c). There are seven major regions with large momentum matrix elements, which are labeled as A, B, C, D, E, F, and G, respectively. We use lower-case letters a, b, c, d, e, f, and g for each transition in these regions, respectively. Region A contains two main transitions a_1 and a_2, as shown in Fig. 2(d). a_1 is the transition from the valence bands 35 and 36 to the conduction bands 41 and 42 in R_1, where both the valence and conduction bands are doubly degenerate. In Table I, we label it as $35, 36 \to 41, 42$. The transition energy of a_1 is about 2.02 eV, which matches the harmonic energy of peak I in Fig. 2(a). The photon energy of peak I is about 0.95 eV. Thus, $2\hbar\omega$ gives 1.90 eV and is nearly equal to the transition energy of a_1. This means that peak I comes from the transition a_1. The transition energy of a_2 is 2.16 eV, which is close to the second-harmonic energy of 2.26 eV for peak II. Therefore, peak II comes from a_2. There is only one transition b in region B, and its transition energy is 2.66 eV. It matches the second-harmonic energy of 2.68 eV for peak III, so peak III is dominated by b. The $|\mathbf{P}|$ for a_1, a_2, and b are 0.03 a.u. (see Table I). This shows that one can attribute each eigenpeak

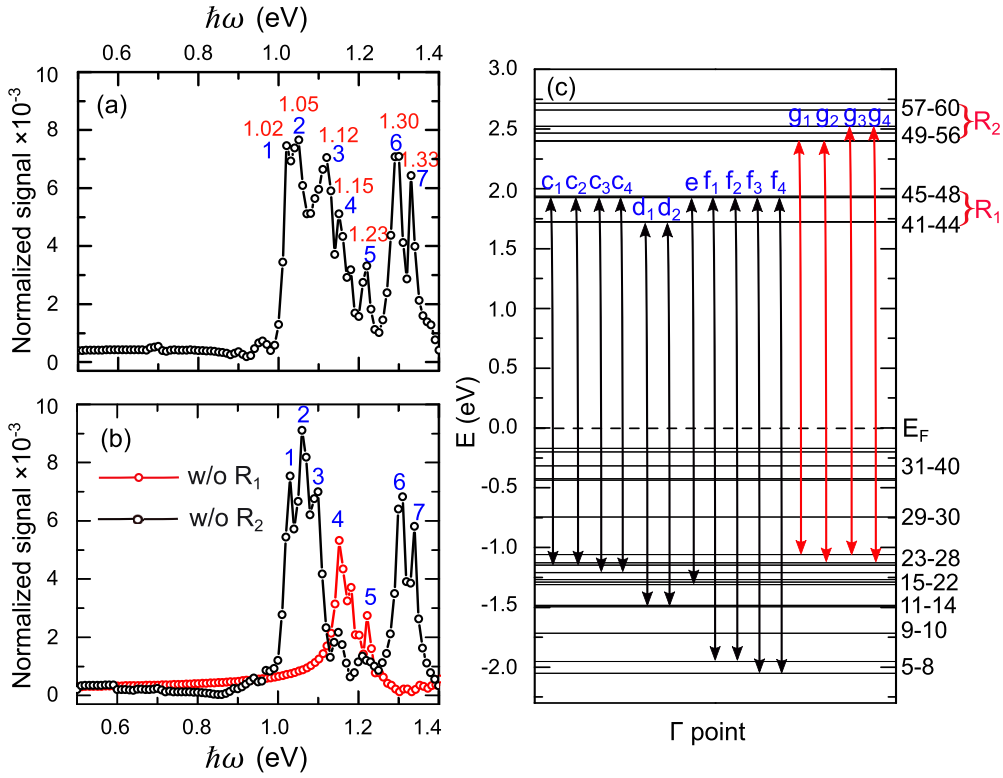

FIG. 3. (a) The third-harmonic spectra as a function of photon energy $\hbar\omega$ at Γ. The blue and red numbers near each peak represent the peak indices and the photon energies, respectively. (b) The third-harmonic spectra as a function of photon energy excluding R_1 (red line) and R_2 (black line) in the conduction bands. (c) The energy diagram at Γ for bilayer $CrCl_3$, where the arrows denote transitions with large **P**, and the letters on the arrow label different transitions.

down to a specific transition, where the nonzero momentum matrix elements are essential.

IV. GOING BEYOND THE SECOND ORDER AND ESTABLISHING A PHYSICAL PICTURE

The above finding is also true for the third-harmonic spectra. From the above discussion, a physical picture is emerging. The harmonic response $\mathcal{R}$ is related to the momentum matrix products [45]

$$\mathcal{R}^{(n)}(t) \propto \underbrace{\mathbf{P}_{ij}\mathbf{P}_{jk}\cdots\mathbf{P}_{lf}}_{n} e^{i(E_f-E_i-n\hbar\omega)t/\hbar}\cdots, \qquad (7)$$

where n is the order of interaction, and the time-dependent exponent highlights the most important term only. Obviously Eq. (5) is overly simplified [45], but it captures the essential physics of the very complex processes during laser excitation as already seen in Eq. (4). This response function replaces the susceptibility $\chi^{(n)}$ in the cw limit. The finding is also true for the third-harmonic spectra. Figure 3(a) shows the third-harmonic spectra at Γ for $CrCl_3$, where the photon energy is scanned from 0.5 to 1.4 eV in steps of 0.01 eV. The first peak is at 1.02 eV, followed by six additional peaks 2–7. Peaks 1–3, 6, and 7 have comparable amplitudes, while peaks 4 and 5 are relatively small. Figure 3(b) presents two sets of data: one excludes R_1 and the other excludes R_2. When only R_1 is excluded (the red line), the original peaks 1, 2, and 3 disappear. Peaks 6 and 7 are largely reduced, while peaks 4 and 5 are almost unchanged. This indicates that peaks 1–3, 6, and 7 are dominated by the transitions between the valence bands and conduction bands in R_1. When we only exclude R_2 (the black line), peaks 1–3, 6, and 7 remain almost unchanged, but peaks 4 and 5 are sharply reduced. This means that those transitions are closely related to peaks 4 and 5. When we only exclude R_3, seven peaks are unchanged, indicating that these peaks are dominated by R_1 and R_2.

Recall Fig. 2(c), where we have five regions C–G with large momentum matrix elements $|\mathbf{P}|$ between the valence bands and conduction bands in R_1 and R_2. Figure 3(c) shows the energy diagram and five regions from C to G, each of which has multiple transitions. Region C contains four transitions: c_1, c_2, c_3, and c_4, as shown in Fig. 3(c) and Table I. The transition energy of c_1 is about 3.07 eV, which matches the third-harmonic energy of 3.06 eV for peak 1 in Fig. 3(a). This shows that peak 1 mainly comes from the transition c_1. The transition energy of c_2 is only 0.01 eV larger than that of c_1, so it also contributes to peak 1. Comparing with c_1 and c_2, c_3 and c_4 have slightly larger transition energies of 3.14 and 3.15 eV, which generate peak 2 with $3\hbar\omega = 3.15$eV. The absolute value of $|\mathbf{P}|$ for c_1 and c_2 is about 0.18 and 0.15 a.u. (see Table I). The other two transitions c_3 and c_4 have almost equal $|\mathbf{P}|$ with the values of 0.13 and 0.15 a.u., respectively, which explains their comparable amplitudes of peaks 1 and 2, as shown in Fig. 3(a). Region D contains two transitions d_1 and d_2, as shown in Fig. 3(c). The corresponding transition energies are 3.20 and 3.21 eV, which contribute to peak 2. The transitions d_1 and d_2 have a smaller $|\mathbf{P}|$ of 0.11 a.u. Region E has only one transition e, and the corresponding transition

energy is 3.26 eV. It matches the harmonic energy of peak 3, where $3\hbar\omega = 3.36$eV. The $|\mathbf{P}|$ of this transition is 0.09 a.u., which is smaller than those of peaks 1 and 2. This leads to the amplitude of peak 3 being smaller than those of peaks 1 and 2. For region F, there are four transitions $f_1 - f_4$ with the transition energies of 3.88, 3.89, 3.98, and 3.99 eV, respectively. These transition energies are close to the harmonic energies of peaks 6 and 7 with $3\hbar\omega = 3.90$ and 3.99 eV, indicating that these two peaks are mainly from the transitions $f_1 - f_4$ [see Fig. 3(c)]. The corresponding $|\mathbf{P}|$ are 0.11, 0.11, 0.12, and 0.11 a.u., respectively. It is found that the $|\mathbf{P}|$ of peaks 6 and 7 is almost equal, so the amplitudes of these two peaks are also close, as shown in Fig. 3(a).

As shown in Fig. 2(c), we can see that only one region G related to R_2 has large momentum matrix elements. It mainly contains four transitions g_1, g_2, g_3, and g_4, as shown in Fig. 3(c) and Table I. Their transition energies are 3.46, 3.53, 3.56, and 3.65 eV, respectively. The first three transition energies almost match the harmonic energy of peak 4 with $3\hbar\omega = 3.45$eV. This indicates that these three transitions contribute to peak 4. This is the reason why peak 4 is so broad. However, only one transition g_4 contributes to peak 5 with $3\hbar\omega = 3.69$eV, giving rise to a narrow peak in comparison with peak 4. In addition, the momentum matrix elements $|\mathbf{P}|$ of $g_1 - g_3$ are 0.23, 0.20, and 0.13 a.u., respectively. By contrast, g_4 has a slightly smaller $|\mathbf{P}|$ of 0.11 a.u. As a result, the amplitude of peak 5 is smaller than that of peak 4.

It is found that the amplitudes of eigenpeaks for the third-harmonic spectra are larger than those for the second-harmonic spectra. The appearance of the strong eigenpeaks needs large $|\mathbf{P}|$. In fact, $|\mathbf{P}|$ in regions C–G did have much larger values than those in regions A and B, as shown in Fig. 2(c). The underlying physics comes from the fact that $|\mathbf{P}|$ contributing to the second-harmonic spectra are related to the valence bands 29–40 and the conduction bands in R_1, which are mainly dominated by the same Cr-d orbitals, as shown in Fig. 1(b). However, $|\mathbf{P}|$ for the third-harmonic spectra involves a larger energy difference. The corresponding valence bands are much lower, which are mainly from the Cl-p orbitals and are denoted as bands 1–28 in Fig. 1(b). Compared to $|\mathbf{P}|$ related to the second-harmonic spectra, $|\mathbf{P}|$ for the third-harmonic spectra would be much larger as the transitions belong to different orbitals. Our calculated momentum matrix elements confirm this conclusion (see Table I for more details).

V. CONCLUSIONS

We have demonstrated that the nonlinear harmonic spectra in a group of bilayers CrX_3 can pinpoint specific transitions between valence and conduction bands. We scan over 100 photon energies from 0.3 to 1.4 eV in fine steps. We map out the momentum transition matrix elements and calculate the corresponding contributions to the harmonic spectra. By including and excluding some transitions, we can directly correlate each peak in both the second- and third-harmonic spectra to a specific transition, which has not been possible previously because often only one- or two-photon energies are used. The first resonance peak in the second-harmonic spectra serves as the onset of the band gap of a material. Complex peaks can now be attributed to the intrinsic electronic properties. All the results are further confirmed by the third-harmonic spectra. Our findings unleash the power of nonlinear harmonic spectra to study the vdW antiferromagnets, and they are likely to motivate future experimental studies beyond CrI_3 [16].

ACKNOWLEDGMENTS

This work was supported by the National Science Foundation of China under Grant No. 11874189. G.P.Z. was supported by the US Department of Energy under Contract No. DE-FG02-06ER46304. The research used resources of the National Energy Research Scientific Computing Center, which is supported by the Office of Science of the US Department of Energy under Contract No. DE-AC02-05CH11231.

[1] Z. Wang, M. Gibertini, D. Dumcenco, T. Taniguchi, K. Watanabe, E. Giannini, and A. F. Morpurgo, Nat. Nanotechnol. **14**, 1116 (2019).
[2] W. J. Chen, Z. Y. Sun, Z. J. Wang, L. H. Gu, X. D. Xu, S. W. Wu, and C. L. Gao, Science **366**, 983 (2019).
[3] T. C. Song, X. H. Cai, M. W. Tu, X. O. Zhang, B. Huang, N. P. Wilson, K. L. Seyler, L. Zhu, T. Taniguchi, K. Watanabe, M. A. McGuire, D. H. Cobden, D. Xiao, W. Yao, and X. D. Xu, Science **360**, 1214 (2018).
[4] D. R. Klein, D. MacNeill, J. L. Lado, D. Soriano, E. Navarro-Moratalla, K. Watanabe, T. Taniguchi, S. Manni, P. Canfield, J. Fernández-Rossier, and P. Jarillo-Herrero, Science **360**, 1218 (2018).
[5] Z. Wang, I. Gutiérrez-Lezama, N. Ubrig, M. Kroner, M. Gibertini, T. Taniguchi, K. Watanabe, A. Imamoğlu, E. Giannini, and A. F. Morpurgo, Nat. Commun. **9**, 2516 (2018).
[6] B. Huang, G. Clark, D. R. Klein, D. MacNeill, E. Navarro Moratalla, K. L. Seyler, N. Wilson, M. A. McGuire, D. H. Cobden, D. Xiao, W. Yao, P. Jarillo-Herrero, and X. Xu, Nat. Nanotechnol. **13**, 544 (2018).
[7] S. Jiang, J. Shan, and K. F. Mak, Nat. Mater. **17**, 406 (2018).
[8] T. Li, S. Jiang, N. Sivadas, Z. Wang, Y. Xu, D. Weber, J. E. Goldberger, K. Watanabe, T. Taniguchi, C. J. Fennie, K. F. Mak, and J. Shan, Nat. Mater. **18**, 1303 (2019).
[9] T. Song, Z. Fei, M. Yankowitz, Z. Lin, Q. Jiang, K. Hwangbo, Q. Zhang, B. Sun, T. Taniguchi, K. Watanabe, M. A. McGuire, D. Graf, T. Cao, J. H. Chu, D. H. Cobden, C. R. Dean, D. Xiao, and X. Xu, Nat. Mater. **18**, 1298 (2019).
[10] S. Mondal, M. Kannan, M. Das, L. Govindaraj, R. Singha, B. Satpati, S. Arumugam, and P. Mandal, Phys. Rev. B **99**, 180407(R) (2019).
[11] N. Sivadas, S. Okamoto, X. Xu, C. J. Fennie, and D. Xiao, Nano Lett. **18**, 7658 (2018).

[12] P. H. Jiang, C. Wang, D. C. Chen, Z. C. Zhong, Z. Yuan, Z. Y. Lu, and W. Ji, Phys. Rev. B **99**, 144401 (2019).

[13] B. Huang, G. Clark, E. Navarro-Moratalla, D. R. Klein, R. Cheng, K. L. Seyler, D. Zhong, E. Schmidgall, M. A. McGuire, D. H. Cobden, W. Yao, D. Xiao, P. Jarillo-Herrero, and X. D. Xu, Nature (London) **546**, 270 (2017).

[14] S. W. Jiang, L. Z. Li, Z. F. Wang, J. Shan, and K. F. Mak, Nat. Electron. **2**, 159 (2019).

[15] K. L. Seyler, D. Zhong, D. R. Klein, S. Y. Gao, X. O. Zhang, B. Huang, E. Navarro-Moratalla, L. Yang, D. H. Cobden, M. A. McGuire, W. Yao, D. Xiao, P. Jarillo-Herrero, and X. D. Xu, Nat. Phys. **14**, 277 (2018).

[16] Z. Y. Sun, Y. F. Yi, T. C. Song, G. Clark, B. Huang, Y. W. Shan, S. Wu, D. Huang, C. L. Gao, Z. H. Chen, M. McGuire, T. Cao, D. Xiao, W. T. Liu, W. Yao, X. D. Xu, and S. W. Wu, Nature (London) **572**, 497 (2019).

[17] W. S. Song, R. X. Fei, L. H. Zhu, and L. Yang, Phys. Rev. B **102**, 045411 (2020).

[18] G. Ndabashimiye, S. Ghimire, M. Wu, D. A. Browne, K. J. Schafer, M. B. Gaarde, and D. A. Reis, Nature (London) **534**, 520 (2016).

[19] H. Z. Liu, Y. L. Li, Y. S. You, S. Ghimire, T. F. Heinz, and D. A. Reis, Nat. Phys. **13**, 262 (2017).

[20] G. P. Zhang, Phys. Rev. Lett. **95**, 047401 (2005).

[21] G. P. Zhang, M. S. Si, M. Murakami, Y. H. Bai, and T. F. George, Nat. Commun. **9**, 3031 (2018).

[22] G. P. Zhang and Y. H. Bai, Phys. Rev. B **101**, 081412(R) (2020).

[23] G. P. Zhang and Y. H. Bai, Phys. Rev. B **103**, L100407 (2021).

[24] M. Ferray, A. L'Huillier, X. F. Li, L. A. Lompre, G. Mainfray, and C. Manus, J. Phys. B **21**, L31 (1988).

[25] G. Vampa, C. R. McDonald, G. Orlando, D. D. Klug, P. B. Corkum, and T. Brabec, Phys. Rev. Lett. **113**, 073901 (2014).

[26] S. Ghimire, A. D. DiChiara, E. Sistrunk, P. Agostini, L. F. DiMauro, and D. A. Reis, Nat. Phys. **7**, 138 (2011).

[27] E. N. Osika, A. Chacón, L. Ortmann, N. Suárez, J. A. Pérez-Hernández, B. Szafran, M. F. Ciappina, F. Sols, A. S. Landsman, and M. Lewenstein, Phys. Rev. X **7**, 021017 (2017).

[28] X. Liu, X. Zhu, X. Zhang, D. Wang, P. Lan, and P. Lu, Opt. Express **25**, 29216 (2017).

[29] M. X. Guan, C. Lian, S. Q. Hu, H. Liu, S. J. Zhang, J. Zhang, and S. Meng, Phys. Rev. B **99**, 184306 (2019).

[30] L. Jia, Z. Y. Zhang, D. Z. Yang, Y. Q. Liu, M. S. Si, G. P. Zhang, and Y. S. Liu, Phys. Rev. B **101**, 144304 (2020).

[31] L. Jia, Z. Y. Zhang, D. Z. Yang, M. S. Si, and G. P. Zhang, Phys. Rev. B **102**, 174314 (2020).

[32] L. Jia, Y. Song, M. S. Si, J. L. Yao, and G. P. Zhang, Phys. Rev. B **105**, 214309 (2022).

[33] J. P. Perdew, K. Burke, and M. Ernzerhof, Phys. Rev. Lett. **77**, 3865 (1996).

[34] P. Hohenberg and W. Kohn, Phys. Rev. **136**, B864 (1964).

[35] G. P. Zhang, Y. H. Bai, and T. F. George, Phys. Rev. B **80**, 214415 (2009).

[36] P. Blaha, K. Schwarz, F. Tran, R. Laskowski, G. K. H. Madsen, and L. D. Marks, J. Chem. Phys. **152**, 074101 (2020).

[37] B. Morosin and A. Narath, J. Chem. Phys. **40**, 1958 (1964).

[38] M. A. McGuire, H. Dixit, V. R. Cooper, and B. C. Sales, Chem. Mater. **27**, 612 (2015).

[39] G. P. Zhang, W. Hübner, G. Lefkidis, Y. H. Bai, and T. F. George, Nat. Phys. **5**, 499 (2009).

[40] K. Blum, *Density Matrix, Theory and Applications* (Plenum, New York, 1981).

[41] W. Schafer and M. Wegner, *Semiconductor Optics and Transport Phenomena* (Springer-Verlag, Berlin, 2002).

[42] M. Murakami, G. P. Zhang, and S.-I. Chu, Phys. Rev. A **95**, 053419 (2017).

[43] M. J. Klein, Am. J. Phys. **20**, 65 (1952).

[44] Y. R. Shen, *The Principles of Nonlinear Optics* (Wiley, New York, 1984).

[45] P. N. Butcher and D. Cotter, *The Elements of Nonlinear Optics* (Cambridge University Press, Cambridge, 1990).

[46] R. W. Boyd, *Nonlinear Optics* (Elsevier Science, Amsterdam, 2003).

[47] W. S. Song, G. Y. Guo, S. Huang, L. Yang, and L. Yang, Phys. Rev. Appl. **13**, 014052 (2020).

[48] Y. Q. Liu, M. S. Si, and G. P. Zhang, Phys. Rev. A **108**, 033514 (2023).

[49] V. K. Gudelli and G.-Y. Guo, Chin. J. Phys. **68**, 896 (2020).

[50] D. E. Aspnes, Phys. Rev. B **6**, 4648 (1972).

[51] Q. Ma, A. G. Grushin, and K. S. Burch, Nat. Mater. **20**, 1601 (2021).

[52] G. B. Ventura, D. J. Passos, J. M. B. Lopes dos Santos, J. M. V. P. Lopes, and N. M. R. Peres, Phys. Rev. B **96**, 035431 (2017).

[53] R. Leitsmann, W. G. Schmidt, P. H. Hahn, and F. Bechstedt, Phys. Rev. B **71**, 195209 (2005).

[54] S. Acharya, D. Pashov, A. N. Rudenko, M. Rösner, M. v. Schilfgaarde, and M. I. Katsnelson, npj 2D Mater. Appl. **6**, 33 (2022).

[55] See Supplemental Material at http://link.aps.org/supplemental/10.1103/PhysRevB.109.094301 for more details on the theoretical methods, the electronic structures, and HHG for bilayers CrX_3. We also demonstrate the results of cw SHG and the third-harmonic spectra for CrX_3. In addition, the underlying physics of eigenpeaks for the nonlinear harmonic spectra of $CrBr_3$ and CrI_3 is discussed, which also includes Refs. [56–60].

[56] J. E. Sipe and E. Ghahramani, Phys. Rev. B **48**, 11705 (1993).

[57] C. Aversa and J. E. Sipe, Phys. Rev. B **52**, 14636 (1995).

[58] J. L. P. Hughes and J. E. Sipe, Phys. Rev. B **53**, 10751 (1996).

[59] G. Kresse and J. Furthmüller, Phys. Rev. B **54**, 11169 (1996).

[60] G. Kresse and D. Joubert, Phys. Rev. B **59**, 1758 (1999).